Omnidirectional and Multi-Material In Situ 3D Printing Using Acoustic Levitation

Hongyi Chen,* Shubhi Bansal, Diego Martinez Plasencia, Lucy Di-Silvio, Jie Huang, Sriram Subramanian, and Ryuji Hirayama

Additive manufacturing is critical in modern production with advanced applications across various domains. However, achieving omnidirectional printing that can adapt to varying substrate geometries is still a challenge. Moreover, multi-material in situ printing without cross-contamination presents another hurdle. In this study, an acoustophoretic 3D fabrication system capable of omnidirectional and multi-material in situ 3D printing is reported using acoustic levitation. This system harnesses a phased array of transducers (PAT) to finely tune the ultrasonic field, generating acoustophoretic forces that levitate and transport objects in mid-air. It allows omnidirectional in situ printing of materials onto complex substrates with diverse orientations in a contactless and voxel-by-voxel manner. It is capable of manipulating a broad spectrum of materials, including liquids with zero-shear viscosities from 1 to 5,000,000 mPa·s, as well as solids. AcoustoFab has successfully printed structural, conductive, and biological materials in varying directions on complex substrates. Additionally, the contactless approach enables in situ printing safely on a delicate surface, as demonstrated by printing on a human hand. The flexibility and versatility of this approach demonstrate promising applications in areas ranging from biomedical engineering to industrial manufacturing.

1. Introduction

Acoustophoresis is a non-contact and label-free (i.e., non-reliance on magnetic or chemical tags) technique, using controlled ultrasound to allow manipulation of materials with high accuracy.[1] It is material-agnostic, capable of manipulating any material within sound-propagating mediums (e.g., water and air).[2,3] The most common use of acoustophoresis in fabrication is to align materials into specific patterns inside a liquid medium[4]

allowing instant particle assembly into arbitrary shapes[5,6] or the creation of microscale composites inside printed structures.[7–10] While acoustic patterning of a wide range of materials (i.e., glass fibers,[11] conductive materials,[9] polymer microparticles,[6] cells[12,13]) has been demonstrated, its scalability and ability to integrate multiple materials remain challenging.[14]

Acoustic levitation is an acoustophoretic technique that levitates and manipulates different types of materials against gravity in mid-air using acoustic radiation forces.[15–22] It has the advantages of material versatility, contactless manipulation, and precise positional control.[19,23] However, it has seen limited applications in additive manufacturing. Acoustic levitation has been used to statically suspend droplets, facilitating the manual injection and embedding of materials such as proteins or nanoparticles into these suspended droplets.[24,25] However, the size of these multicompartment droplets is restricted to the millimeter range, limiting their scalability for complex additive manufacturing applications. Another attempt relies on external mechanical attachments (i.e., a robotic arm) to move the entire levitation system for positioning levitated beads and sticks assembling them with UV glue.[26] However, this setup requires a large empty space around printed objects and the device. Challenges remain in allowing any acoustic scattering substrates or scalable printed objects in the acoustic levitation field, as such

H. Chen, S. Bansal, D. M. Plasencia, S. Subramanian, R. Hirayama
Department of Computer Science
University College London
London NW1 2AE, UK
E-mail: hongyi.chen.16@ucl.ac.uk

The ORCID identification number(s) for the author(s) of this article can be found under https://doi.org/10.1002/admt.202401792

L. Di-Silvio
Faculty of Dentistry
Oral & Craniofacial Sciences
King's College London
London SE1 1UL, UK

J. Huang
Department of Mechanical Engineering
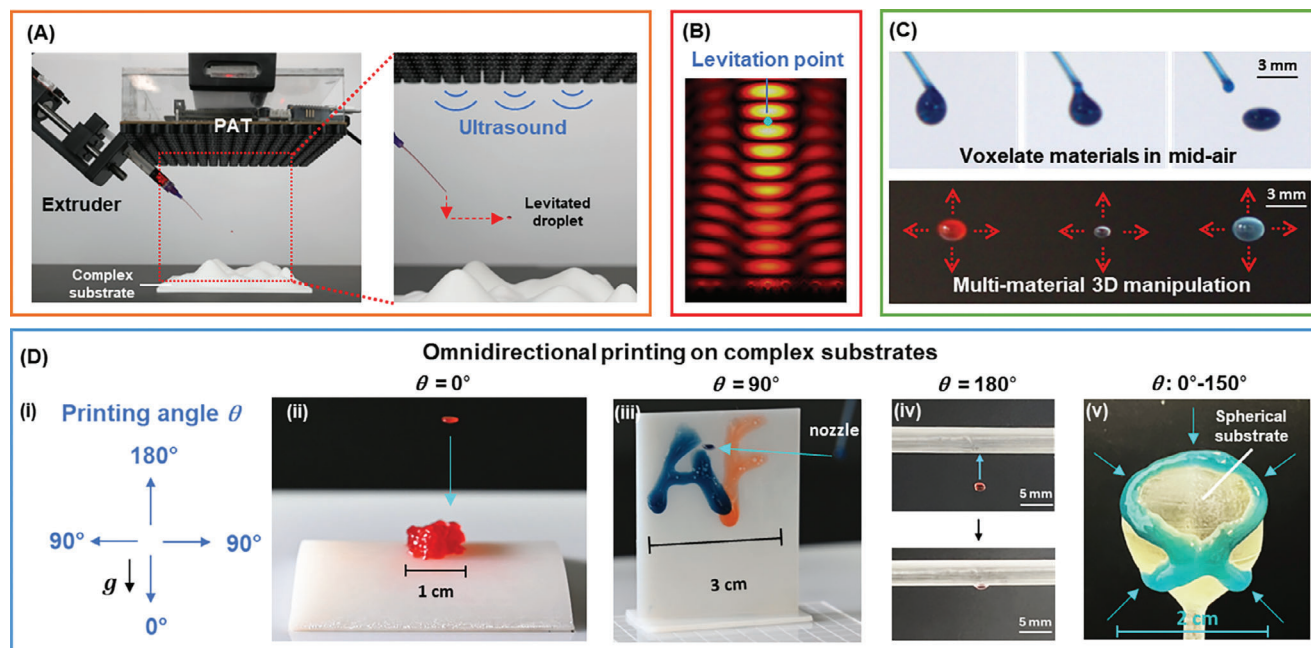University College London
London WC1E 7JE, UK

Figure 1. AcoustoFab system overview. A) The core unit of the AcoustoFab system is the PAT, which can be strategically positioned above substrates to finely tune the sound field within the working space for the controlled creation and movement of levitation traps. Extruders are equipped to introduce materials in the working space. B) Acoustic pressure plot of a levitation trap which levitates objects in mid-air between the high-pressure points. C) Voxelization and 3D manipulation. AcoustoFab is capable of voxelizing extruded materials into droplets and levitating them in mid-air by adjusting the strength, positions, and motions of levitation traps. D) Omnidirectional printing. The system can manipulate and transport multi-material droplets contactlessly, enabling in situ printing on non-planar substrates with various orientations in an omnidirectional manner. i) The printing angle θ is defined as the angle between the directions of deposition and gravity **g**. AcoustoFab is capable of printing at 0° on a horizontal surface ii), 90° on a vertical surface iii), and 180° upwards on a horizontal cylinder iv). θ can be dynamically adjusted for each voxel for printing around a sphere v).

objects lead to distortion of the sound field and cause objects to shake or drop. Although a recent study has demonstrated full 3D manipulation of materials with such scattering objects in the working space relying only on acoustic levitation[27] no existing work has utilized this approach for additive manufacturing to date.

In this work, we present AcoustoFab, a fabrication system that utilizes acoustic levitation for omnidirectional and multi-material in situ printing on complex and non-planar surfaces of diverse orientations as seen in **Figure 1** and Supplementary Video 1. Our system utilizes a phased array of transducers (PAT) to precisely control the ultrasound field within the operational volume alongside stationary extruders for adding materials (Figure 1A). PAT can effectively generate and move acoustic levitation traps (Figure 1B) even in proximity to sound-scattering objects, to voxelize extruded materials into droplets and transport them in any direction, overcoming gravity (Figure 1C). This capability enables in situ printing on complex substrates of diverse orientations in an omnidirectional manner, even directly opposite to gravity (Figure 1D). It surpasses constraints of traditional 3D printing on printing directions, substrate orientation, and the dependency on flat substrates. Using acoustic levitation to transport extruded inks from fixed extruders eliminates the necessity for dedicated 3D mechanical stages or device movement within the workspace, streamlining the material addition process. Additionally, the contactless approach also minimizes the risk of cross-contamination from nozzles and allows safe in situ printing on fragile substrates.

2. Operating Principles of AcoustoFab

The AcoustoFab generates acoustophoretic force F_a on the z axis between the object and the center, assuming the Gor'kov model[28] (object radius $R \ll$ acoustic wavelength λ). For liquid detachment, the AcoustoFab system creates a levitation trap $\lambda/4$ ($\approx$2 mm) below the nozzle tip. When the liquid is being extruded, F_a acts downward to help the gravitational force F_g overcome the capillary force F_c to detach the nozzle.[29] Once the liquid droplet is detached, F_a acts upward to suspend the droplet against F_g. Note here that $F_c = \pi \sigma d$[30] $F_g = -V\rho g$, and $F_a \propto VP^2$, where σ is the liquid surface tension, d is the nozzle diameter, V is the droplet volume, ρ is the liquid density, g is the gravitational acceleration, and P is the acoustic pressure of the trap. To successfully detach and trap a liquid droplet, it is important to appropriately control the acoustic pressure P. P needs to be high enough to create sufficient acoustic force F_a necessary both for detaching the droplet from the nozzle and counteracting the droplet's gravity once it is detached (see **Figure 2B**). On the other hand, if acoustic pressure P is too strong, the acoustic force F_a has a risk to cause droplet atomization.[31]

We experimentally evaluated the levitation characteristics using three types of liquid materials: water ($\sigma = 72.8$ mN m^{-1}, $\mu = 1$ mPa·s), glycerol ($\sigma = 63.4$ mN m^{-1}, $\mu = 1412$ mPa·s), and isopropanol ($\sigma = 20.8$ mN m^{-1}, $\mu = 2.3$ mPa·s), which are Newtonian fluids with a range of viscosities and surface tensions. Figure 2C shows the levitation window (the minimum and the maximum values of the droplet volume available, $V_{\min}$
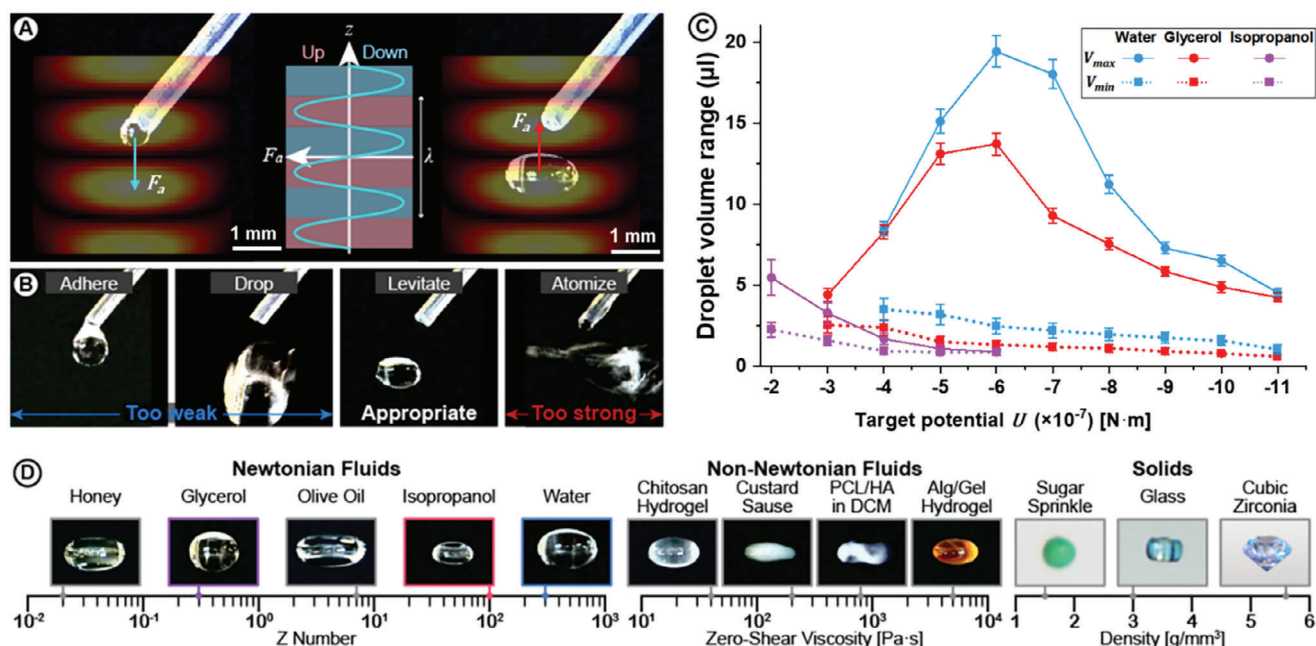
Figure 2. Multi-material voxelization assessment. A) Illustration of the acoustic trap generated just below the nozzle. The acoustic force F_a depends on the droplet position and is used to detach and levitate the droplet extruded. B) Four situations in the droplet detachment process, depending on the strength of F_a. Appropriate F_a needs to be applied for successful detachment. C) The levitation window of water, glycerol, and alcohol in terms of droplet volume range and the target potential U. D) The range of materials that can be levitated in the AcoustoFab system from fluids to solids.

and V_{max}) of these droplets in AcoustoFab, with a range of target potential U ($\propto -P^2$). As U decreases, the strength of acoustic trap increases, thereby decreasing the required F_g for detachment and the V_{min} of all three liquids. The decrease in U increases V_{max} of water and glycerol up to a threshold because it results in a stronger F_a that allows levitating heavier droplets. After the threshold, V_{max} starts decreasing due to droplet atomization caused by too strong F_a. For isopropanol, V_{max} decreases with the decrease of U without such a peak. As the volume of the isopropanol droplet increases, atomization occurs before its gravity supersedes F_a due to its lowest surface tension. The surface tensions of glycerol and water are quite similar, but their viscosities differ by more than a factor of 1000. Despite this vast difference in viscosity, the trends observed in both liquids are similar, indicating that viscosity does not significantly impact the levitation window.

Z value, which is defined as $Z = \sqrt{2\rho\sigma R}/\mu$, is often used for quantifying the printability of droplet-based printing techniques. For drop-on-demand inkjet printing, the printing window of $1 < Z < 14$.[32] The acoustophoretic force in AcoustoFab aids in detaching extruded material from the nozzle and efficient voxelization. This enables AcoustoFab to handle a wider range of liquids and even solids as shown in Figure 2D. In terms of levitating Newtonian fluids, it has been shown to cover a wide range of Z values (1×10^{-2}-3×10^2) can levitate honey and olive oil in addition to the three Newtonian fluids used in the evaluation. For non-Newtonian fluids, it can levitate fluids with zero-shear viscosity up to 5×10^6 mPa·s, including hydrogels (chitosan) composites (Alg/Gel), and emulsions (custard sauce) and filler-loaded polymer/organic solution inks (hydroxyapatite (HA) loaded polycaprolactone (PCL) in dichloromethane (DCM)). These materials

have been widely used in tissue engineering,[33,34] soft robotics[35] food[36] and wearable electronics.[37] Moreover, it is also capable of levitating solids with a density of up to 5.6 g mm^{-3}, demonstrating its versatility in handling a diverse spectrum of materials.

3. Evaluation of Omnidirectional Printing

Using acoustophoretic force to counteract gravity, PAT enables omnidirectional levitation, movement, and printing of materials. We performed evaluation tests at varying printing angles, including 0°, 90°, and 180° to assess the omnidirectional printing capabilities of the AcoustoFab system. Glycerol droplets were deposited with a range of printing angle θ, which is defined as the angle between the deposition and gravity direction as seen in Figure 1D. Testing printing at 0°, glycerol droplets were moved above the target location and then deposited on a horizontal surface using gravity (**Figure 3A(i)**). By adjusting the sound field, AcoustoFab is capable of voxelizing and subsequent printing of extruded liquids with a range of volume (2-10 µL for glycerol) in a controlled manner, which in turn defines the contact radius r and height h of deposited droplets (Figure 3A(ii)). This volume control is important for applications requiring precise dosing and placement of bioactive agents or other functional materials. The printing accuracy was tested by printing 2.5 µL glycerol droplets into a 7 × 7 grid (side length: 60 mm) onto an acrylic board oriented horizontally. (Figure 3A(iii)). The results (Figure 3A(iv)) show that droplet deposition accuracy is highest at the center of the grid and decreases toward the edges, with displacements primarily directed outward from the center. This consistent displacement trend suggests that further calibration
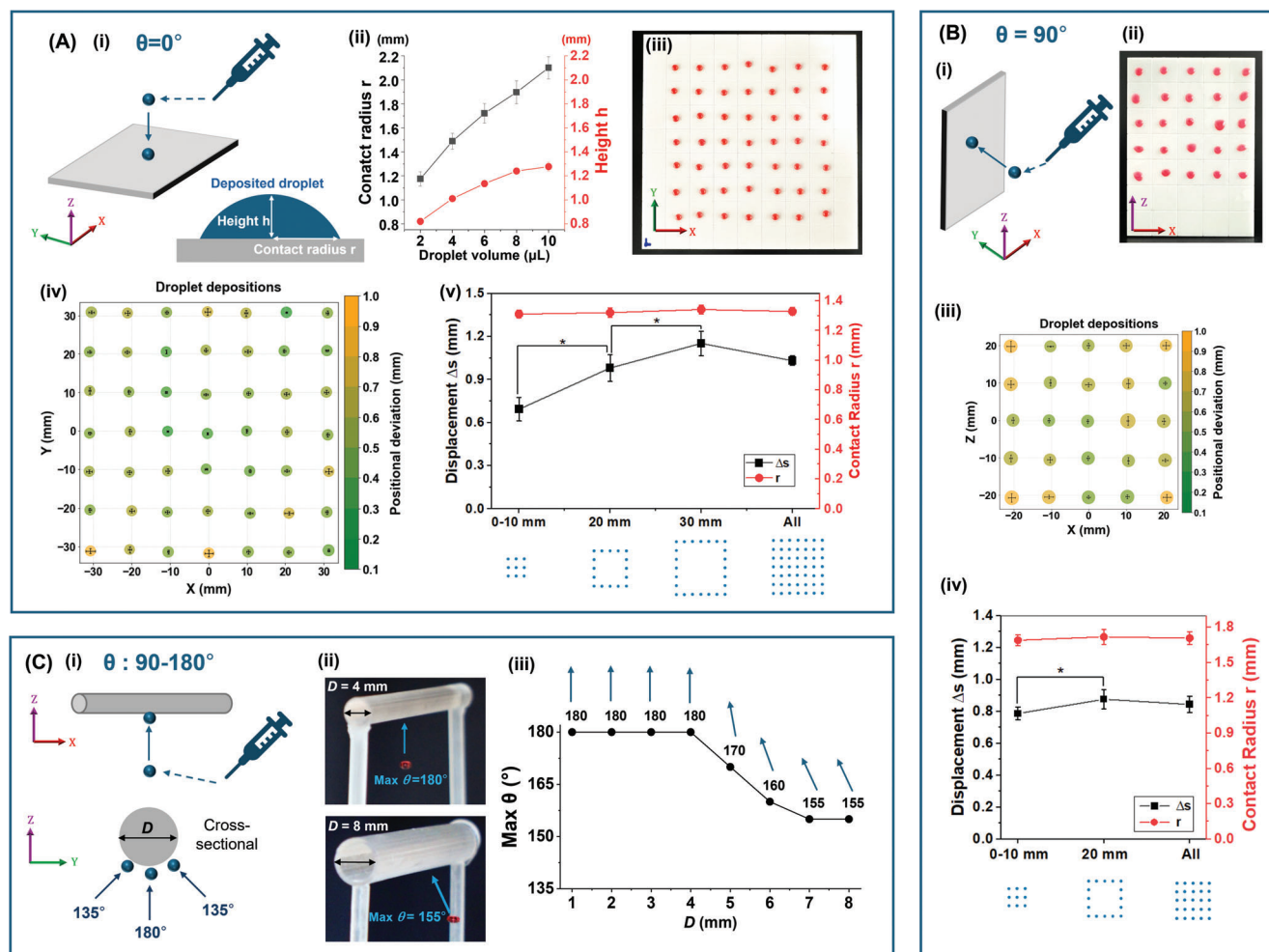
**ADVANCED
SCIENCE NEWS**

www.advancedsciencenews.com

**ADVANCED
MATERIALS
TECHNOLOGIES**

www.advmattechnol.de

Figure 3. Printing evaluation of AcoustoFab at varying printing directions. A) Accuracy assessment of printing at 0°. i) Schematics of printing at 0° on a horizontal substrate. ii) Voxelization assessment, the effect of the volume of deposited droplets on their equivalent contact radii and height on a horizontal plane. iii) Glycerol droplets (2.5 μL) printed in 7 × 7 grids (side length; 60) mm onto an acrylic board. iv) Printing accuracy. The centroid and radii of the circles are the average deposition positions and equivalent contact radii of the deposited droplets. The crosses of grids are the target locations. The horizontal and vertical error bars are the standard deviation of the deposition in the X and Y directions and the color of circles signifies the average positional deviation. v) The displacement and equivalent contact radii of the droplets in the 0–10, 20, and 30 mm region. B) Evaluation of printing at 90°. i) Schematics of printing 90° on a vertical substrate. ii) Glycerol droplets printed on a 45 mm × 45 mm grid oriented vertically in 5 × 5 grids. iii) Printing accuracy. iv) The displacement and equivalent contact radii of the droplets in the 0–10, 20, and 30 mm regions. C) Assessment of printing at 90°-180°. i) Schematics of printing upwards on a horizontal cylinder with a diameter of D at different angles. ii) Printing at 180° vertically upwards on a horizontal cylinder. iii) Maximum printing angle for the cylinder with varying D. Statistically significant differences were determined using unpaired two-tailed t-tests as * $p < 0.05$.

could effectively compensate for these deviations using a method similar to that reported by Fushimi, et al.[38] Droplets within the 0–10 mm square revealed a minimal displacement of ≈0.7 mm, which increased to ≈1.1 mm for droplets at the periphery (X or Y = 30 mm), as summarized in Figure 3A(v). There is no significant difference between the average equivalent contact radius of droplets in the different regions indicating a uniformity in droplet size across the locations.

The PAT is capable of generating stable levitation traps in the proximity of large surfaces overcoming their sound scattering by modelling the sound scattering, enabling printing horizontally on a vertical surface. For evaluation of printing at 90°, droplets were printed horizontally onto a vertically oriented acrylic of 5 ×

5 grids (side length: 40 mm) between the height of 20 and 70 mm as seen in Figure 3B(i,ii). The deposition positions, radii, and positional deviations of the deposited droplets in different regions are shown in Figure 3B(iii). Droplets within the 0–10 mm square have significantly lower displacement (0.79 mm) than that in the 20 mm square (0.86 mm), and the average displacement of all droplets is 0.83 mm. The average equivalent contact radius of droplets remains consistent across different regions, indicating a uniform droplet size throughout the locations.

In exploring the limits of the printing angle $θ$ for upward printing, droplets were directed upwards to horizontal cylinders varying in diameter from 1 to 8 mm. For cylinders with diameters up to 4 mm, the maximum printing angle is 180°, directly

**ADVANCED
SCIENCE NEWS**

www.advancedsciencenews.com

**ADVANCED
MATERIALS
TECHNOLOGIES**

www.advmattechnol.de

opposite to gravity. As the cylinder diameter increased to 4 mm and beyond, sound scattering from the cylinder surface presented challenges in forming stable acoustic traps directly underneath. Adjusting the printing angle allows printing from angles below the cylinder. As D increases from 4 to 8 mm, the max θ decreases from 180° to 155°. The results demonstrate robust printing across different orientations and the system's reliability and precision in handling dynamic changes in printing angles.

4. Printing Performance of AcoustoFab

AcoustoFab allows omnidirectional and multi-material printing on complex surfaces of diverse orientations in a voxel-by-voxel and contactless manner. (Video S1, Supporting Information). As seen in **Figure** 4A, AcoustoFab can finely adjust the trajectory of each droplet allowing printing on multiple surfaces of a cuboid, or around the curved surface of a vertical or horizontal cylinder, where the printing angle dynamically changes from 0° to 180° demonstrating its adaptability. Moreover, the system demonstrates its versatility by creating patterns on vertical surfaces (Figure 4B) and a self-standing 3D structure on horizontally oriented convex and undulating surfaces (Figure 4C). This capability allows for the construction of intricate designs and functional structures directly suited to the shape of the underlying surface. A notable application of this technology is demonstrated by its ability to print conductive hydrogel on spherical surfaces to connect electrical components (Figure 4D). Additionally, the system's contactless and omnidirectional printing techniques offer advantages for in situ bioprinting directly on human tissues. This is exemplified by the safe deposition of biocompatible hydrogel droplets onto a human fist (Figure 4E), illustrating the system's potential in medical applications such as personalized therapeutic interventions or complex tissue engineering. As the acoustic waves are mostly reflected (>99.9%) at the droplet surface due to the mismatch in acoustic impedance between air and the hydrogel, fragile cargo, such as cells[39] can be loaded in the hydrogel and printed with high viability.[29] In this study, Acousto-Fab has bioprinted Alg/Gel hydrogel composites embedded with human osteoblast (HOB) cells (Figure 4F). The cross-linked and cell-embedded hydrogel without being subjected to the printing process was used as control. As seen in the qualitative live/dead images, cells remained viable at 10 days as seen in Figure 4F(i). Change in morphology was observed with enlarged cells and focal aggregation which could be attributed to cells entering a differentiated state. The viability of cells in the AcoustoFab printed group shows no significant difference from the control group as seen in Figure 4F(ii). This demonstrates that the acoustophoretic force applied to the hydrogel does not affect the high viability of embedded cells, showing the potential of AcoustoFab in biological applications.

AcoustoFab can simultaneously create and manage multiple levitation traps (Figure S1, Supporting Information), enabling it to manipulate and mix multiple droplets in mid-air (Figure 4G). This capability facilitates multi-material printing of gradient compositions by mixing droplets with varying ratios in mid-air prior to deposition as seen in Figure 4G(i-ii). Hydrogel droplets can be crosslinked in mid-air by mixing with a droplet of crosslinking solution before deposition to enhance its stability. By utilizing multiple nozzles, crosslinked hydrogel beads with different compositions can be printed as seen in Figure 4G(iv-vi). This demonstrates the capability of initiating chemical reactions in mid-air and creating various material composites and gradients for printing. Other printing technologies often require intricate mechanical adjustments to create gradient materials[40,41] and face challenges in promptly altering material reactions without cross-contamination. In contrast, AcoustoFab's contactless, voxel-by-voxel approach allows for precise dynamic switching of chemical reactions with temporal control during the printing process, minimizing contamination and enhancing the integrity and specificity of each reaction.

5. Discussion

The AcoustoFab system introduces a new method in 3D printing. By leveraging acoustic levitation, it addresses the challenges of omnidirectional and multi-material printing, providing a contactless, precise, and versatile solution.

The system's omnidirectional printing ability allows the precise deposition of materials in any direction, overcoming challenges of seamless adaptation to the intricate geometries of various substrates. This flexibility enables precise in situ printing on surfaces that are not only complex but also oriented in diverse directions, thereby expanding the potential for advanced manufacturing applications. Furthermore, multi-material printing capability enhances the system's utility by enabling the simultaneous use of varied materials within a single print job. It is capable of manipulating a broad spectrum of materials, including liquids with zero-shear viscosities from 1 to 5000000 mPa·s, as well as solids. This feature is instrumental in producing structures with customized functionalities, from cell-embedded devices for biomedical applications to advanced composites for technical components. For instance, AcoustoFab has demonstrated the printing of high-viability cell-embedded structures and conductive traces, paving the way for in situ (bio)printing of customized tissue-engineered implants and wearable devices.

In addition, AcoustoFab's contactless printing mechanism ensures that nozzles remain at a safe distance from the substrate, eliminating mechanical stress from nozzles that could potentially damage the substrate or the printed structures. This can benefit delicate applications such as in situ printing wearable electronics or intricate biomedical devices on human tissues. Moreover, the reduced risk of cross-contamination enhances biocompatibility for medical devices and ensures reliability in electronic applications.

The primary component of our system, the phased array transducer (PAT), is a cost-effective and commercially available element. Continued refinement of acoustic field stability is expected to enhance reproducibility as this technology advances, making it more accessible and scalable for broader applications.

In essence, AcoustoFab transforms the approach to handling, depositing, and utilizing materials in additive manufacturing. It addresses difficulties in additive manufacturing, such as enabling omnidirectional printing on complex surfaces, multi-material integration without cross-contamination, and contactless deposition to minimize stress on substrates. It opens up both functional and creative possibilities, from bioprinting to soft robotics and electronics.
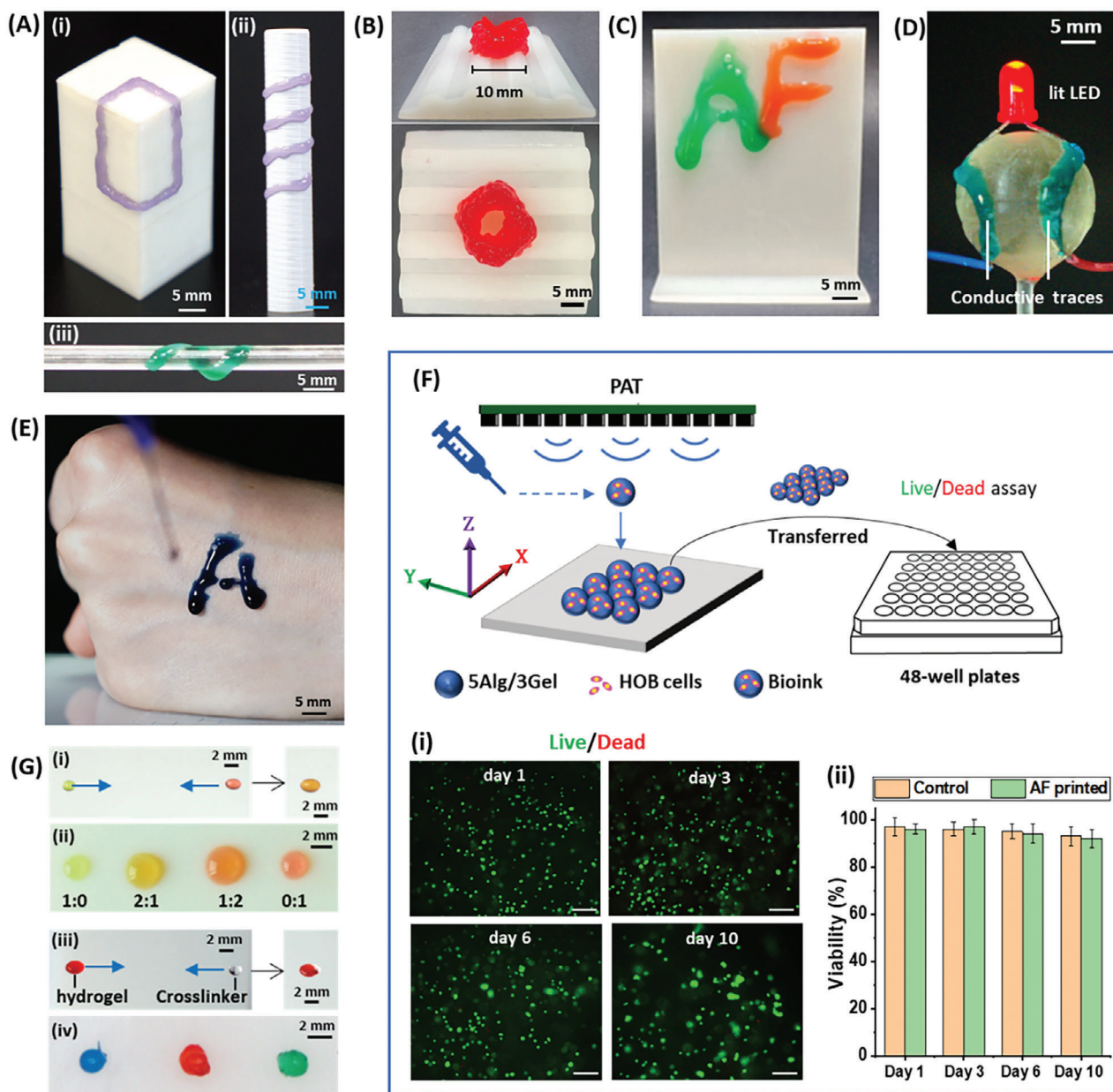
Figure 4. Printing performance of AcoustoFab. A) Printing omnidirectionally on different surfaces of a cuboid (i), around a vertical cylinder (ii), and around a horizontal cylinder (iii). B) 3D printing hydrogel on a convex and wavy surface into a self-standing 3D circular structure. C) Printing the letters "A" and "F" on a vertical surface. D) Printing conductive traces on a sphere that lights up an LED. E) In situ printing of hydrogel on a human fist. F) Bioprinting with AcoustoFab. Bioink droplets of HOB cells-embedded 5Alg/3Gel hydrogel were printed at 0° on a horizontal surface for viability assessment. i) Representative fluorescence micrographs of live (green)/dead (red) HOB cells in crosslinked hydrogel at day 1, 3, 6, and 10 after being printed (scale bar: 200 μm). ii) Viability of HOB cells in control and AF printed group at day 1, 3, 6, and 10 after being printed. Statistical analysis revealed no significant differences in viability between the AcoustoFab printed group and the control group at all observed time points (unpaired two-tailed *t*-tests). G) Droplet mixing in mid-air before deposition. The system can (i) levitate multiple droplets simultaneously and mix them in mid-air, prior to (ii) depositing the mixed droplets at a target location with varying mixing ratios. This technique can also be used to deposit crosslinked hydrogel beads by (iii) mixing droplets of hydrogel and crosslinking solution to crosslink in mid-air, and (iv) depositing them.

6. Experimental Section

Experimental Setup: Acoustophoretic system: The core of AcoustoFab's functionality resides in its phased array of transducers (PAT), which is a grid-like arrangement of 16 × 16 transducers adapted from an open hardware model outlined in reference.[42] Each transducer (HongChang Electronic, HC10T-40TR-P) in this array has a diameter of 10 mm and operates at a consistent frequency of 40 kHz, delivering ≈8.1 Pa at 1 m distance when driven at 20 Vpp. An FPGA board (Waveshare CoreEP4CE10) is used to receive phase and amplitude updates from the CPU using a USB FT245 Asynchronous FIFO Interface at 8 Mb s^{-1}, allowing more than 10000 updates per second. In all the prototypes of the AcoustoFab system

that we built and used in this study, the same PAT was used and aligned on top at 12 cm to the printing substrates. This strategic placement ensures that the ultrasound field permeates throughout the printing space to effectively control droplet deposition.

Automated Extruders: While the PAT plays a key role in manipulating different materials, the introduction of these materials in the working space necessitates dedicated nozzles. AcoustoFab uses a dedicated nozzle for each material. Each nozzle is mounted on a stepper motor (NEMA 17) controlled by a microcontroller (Arduino Nano), and thus its ejection is automated. While other platforms maneuver their nozzles on a 3D stage for deposition, AcoustoFab's nozzles stay fixed. When a nozzle ejects material, AcoustoFab's acoustophoretic platform immediately creates a levitation trap, which then holds, secures, and transports the levitated particle to its intended location. This approach makes it easier to add materials without adding dedicated 3D stages and ensures the nozzle never touches other materials during the printing process, drastically reducing the risk of cross-contamination. Depending on the application, single or multiple nozzles were integrated into the prototypes.

Control Algorithms and Software: Original sound-field control with scattering surfaces: To control acoustic levitation, we need to compute the optimal phases and amplitudes of the transducers. It is important to note that traditional control algorithms of PATs, such as GS-PAT[43] or IBP[17] are unsuitable for our setup as they demand an empty working volume. Therefore, we adapted and modified the control algorithm proposed by Hirayama, et al.[30]

This algorithm[30] uses the model based on the boundary element method (BEM) to represent how complex activations of N transducers ($\tau \in \mathbb{C}^N$) contribute to the complex acoustic pressures at L points of interest in sound fields ($\zeta \in \mathbb{C}^L$) using a linear system: $\zeta = E\tau$, where E can be represented by three matrices as $E = F + GH$. Here, F and G represent the respective contributions from the transducers and mesh elements of the object to the points of interest, and H represents the contribution from the transducers to the mesh elements. Although BEM is usually considered incompatible with real-time applications, this algorithm can compute E in real-time, by computing F and G in parallel depending on the application while pre-computing H once the setup (i.e., transducers and objects) is defined.

Using the linear model above, the algorithm[30] uses a solver to obtain the transducers' activations τ that generate an ideal sound field ζ, which provides the maximum trapping stiffness by minimizing the Gor'kov potential U_t at desired trapping positions r_t. This trapping stiffness metric U_t can be determined by the complex acoustic pressure P_t and its spatial derivatives at the levitation position r_t and constant values (K_1 and K_2) as:[16]

$$U_t = K_1 \left| P_t \right|^2 - K_2 \left(\left| \frac{\partial P_t}{\partial x} \right|^2 + \left| \frac{\partial P_t}{\partial y} \right|^2 + \left| \frac{\partial P_t}{\partial z} \right|^2 \right) \tag{1}$$

This prior work also proposed a simplified version of this metric $U_t = K_1 \left| P_t \right|^2 - K_2 \left| \frac{\partial P_t}{\partial z} \right|^2$ by assuming that the system creates standing wave-like acoustic traps along the z axis because the transducers face downward. Assuming material densities used in this study are much larger than the air density, we used $K_1 = 7.5 \times 10^{-15}$ and $K_1 = 2.1 \times 10^{-20}$. Here, phase-only optimization is assumed (i.e., the amplitudes of the transducers are always maximum), and thus the goal of the optimization is to find the optimum phases of the transducers ($\varphi = [\varphi_1, \ldots, \varphi_N]^T$) that minimize U_t at every trap position. This can be realized by using gradient descent to minimize the following cost function $O(\varphi)$ with a simple step size determined as $-1/\|\nabla O(\varphi)\|_2$.

$$O(\varphi) = \sum_{t=1}^{T} \left[U_t + w_s \left(\bar{U} - U_t \right)^2 \right] \tag{2}$$

Here, the bar (ˉ) represents the mean value among all the T traps, and w_s is a weight coefficient. The second term in this cost function is to equalize the qualities of all T traps by minimizing the standard deviation. The

amplitudes of the transducers ($a = [a_1, \ldots, a_N]^T, 0 \leq a_n \leq 1$) are usually fixed to their maximum (i.e., $a_n = 1$ for every transducer).

It is worth noting that this solver does not allow us to individually control the potential values U_t', because its purpose was to simply minimize them. This is suitable for acoustic manipulation of solid materials, like polystyrene beads, but not for liquid materials handled in our AcoustoFab system. An acoustic trap with too low potential value U_t will most likely atomize the levitated droplet, preventing the liquid handling for printing.

If there is only a single trap to be created (i.e., $T = 1$), the easiest way to control the potential value U_t' could be adjusting the transducers' amplitudes a after minimizing U_t with Equation (2). Assuming all the transducers have the same value A (i.e., $a_n = A$ for every transducer), the potential U_t is proportional to A^2. To realize the target potential U_t^{tar}, we first estimate the potential U_t^{est} assuming the maximum transducer amplitudes ($A = 1$) and then adjusting the transducer amplitude A as $A = \sqrt{U_t^{tar}/U_t^{est}}$. However, this approach cannot be used to control the potential values of multiple traps individually.

Thus, we needed to modify this original solver proposed by Hirayama et al.[30] to realize specific target potential values U_t at multiple trap positions. Note here that the same scattering model can be directly used for our AcoustoFab system without any modification.

The New Solver: The proposed solver consists of three steps: Initial estimation, Iterative phase optimization, and Final amplitude tuning. These three steps allow us to individually control the potential values at multiple levitation traps. We used a reference target potential U^{ref} and target ratio γ_t to represent the target potential value for each point U_t^{tar} as: $U_t^{tar} = U^{ref} \gamma_t$.

Initial estimation: In this step, we first initialize the transducers' phases φ by using the heuristic approach[30] This heuristic approach uses two points per trap, which are at the trap position and the position slightly above it (e.g., $\lambda/32$), with a π radian offset in the target phases and target amplitudes defined by $\sqrt{\gamma_t}$. By simply backpropagating those points with the conjugate transpose of the transmission matrix E^*, we can calculate the transducer phases φ without any iterations. Although this approach is not able to provide optimal phases φ, it can quickly provide good initial phases that can be used in the following step. Following this phase initialization, we compute the initial transducer amplitude A as:

$$A = \sqrt{\frac{U^{ref}}{T} \sum_{t=1}^{T} \frac{\gamma_t}{U_t^{est}}} \tag{3}$$

Iterative phase optimization: After getting the initial transducer phases φ and amplitude A, we then use gradient descent to minimize a new cost function as $O(\varphi)$:

$$O(\varphi) = \sum_{t=1}^{T} \left(U_t - U^{ref} \gamma_t \right)^2 \tag{4}$$

An advantage of using this new cost function compared to the original (Equation (2)) is its capability to control individual target potential for each levitation trap. In addition, it does not require tuning any weighting factors like w_s. In this study, we used the number of iterations $K = 200$.

Final Amplitude Tuning: After the iterative phase optimization, this step defines the final transducer amplitude A as the same as Equation (3) but with the optimized transducer phases φ.

Update Interface: The new solver was implemented using OpenCL similarly to the solvers (e.g., GS-PAT[43] or IBP[17]) implemented in the OpenMPD platform[42] so that ours also can be integrated into this open platform to fully utilize the standardized update engine and driver. This engine facilitates the creation of levitation traps and focal points along specific manipulation paths while ensuring a constant update rate of the PAT boards (e.g., 10000 updates per second).

For controlling the stepper motors for automated ejection and leveler control, we simply used the serial communication protocol. We implemented the ejection control software using C++ and integrated it into the

**ADVANCED
SCIENCE NEWS**

www.advancedsciencenews.com

**ADVANCED
MATERIALS
TECHNOLOGIES**

www.advmattechnol.de

OpenMPD software, allowing us to control the PAT board and ejection simultaneously.

Material Preparations: Isopropanol (99.9%, Hexeal), Glycerol (G5516, Sigma-Aldrich), sugar sprinkles (B Kosher), honey (Rowse), glass beads (TOAOB), cubic zirconia (The Curious Gem) and transparent UV resin (clear impact, Liqcreate, Utrecht, The Netherlands) were used as received.

Hydrogel Inks: Sodium alginate (A2033), chitosan (448869), and gelatin (type A, 90–110 bloom derived from porcine skin) were purchased from Sigma Aldrich. Polyacrylamide (Mw: ≈15 Mio. g mol^{-1}, Carl Roth) was purchased from techmate. Alginate/gelatin (Alg/Gel) hydrogel composite was used as printing inks due to its desired rheological properties for extrusion and shape-retaining, and excellent biocompatibility in promoting cell viability and function.[44] To prepare the composites, alginate powders were first dissolved in deionized water under magnetic stirring at ≈500 rpm and 50 °C for 2 h. Then gelatin powders were added to the alginate hydrogel under magnetic stirring at ≈ 200 rpm and 50 °C for another 2 h. Prior to printing, the hydrogel composites were loaded into syringes and centrifuged (2000 rpm) for 3 min to remove air bubbles. Conductive hydrogel was prepared by first mixing 65% w/v LiCl in DI water under magnetic stirring at 400 rpm for 20 min, and then mixing polyacrylamide in the LiCl water solution under magnetic stirring at 400 rpm for 1 h.

Bioink: Human osteoblast (HOB) cells (PromoCell Cat. No: C-12720) were cultured in Dulbecco's modified Eagle's medium (D6046, Sigma) supplemented with 10% fetal bovine serum (F9665, Sigma) and 1% penicillin-streptomycin (P0781, Sigma). To make the bioink, HOB cells were mixed with 5Alg/3Gel hydrogel composite at a density of 2×10^6 cells ml^{-1} with gentle pipetting. The preparation and printing of the bioink were carried out at a temperature of 37 °C to preserve cell viability and reduce viscosity to a fluid-like state, facilitating voxelization and levitation. The composition of 5Alg/3Gel was used as it offers a balance between viscosity for fabrication and cell viability.[44] The bioink was centrifuged at 300 rpm for 2 min to remove air bubbles while maintaining the dispersion of cells in the hydrogel. 100 mM CaCl$_2$ solution was used to crosslink the hydrogel.

Filler-Loaded Polymer/Organic Solvent Ink: Hydroxyapatite nanoparticles (HA) loaded polycaprolactone (PCL) in dichloromethane (DCM) ink was used to demonstrate AcoustoFab's capability of manipulating polymer/organic solvent ink systems which have been used for biomedical applications.[45,46] HA nanoparticles (60 nm ± 10 nm) and PCL pallets (molecular weight: 80 kDa) were purchased from Sigma-Aldrich and DCM (≥99.9% stabilized) was purchased from VWR. To make the ink, 25% w/v HA was first dispersed in DCM under magnetic stirring (500 rpm), and then 20% w/v PCL pallets were dissolved in the dispersion under magnetic stirring (200 rpm) for 2 h.

Evaluations of Levitation: Levitation of different extruded droplets: To obtain the results summarized in Figure 2C, we used the setup illustrated in Fig S2. In this setup, an automated extruder and a high-resolution camera (ELP 4K Webcam) were attached to a single-sided levitation system to capture droplet ejection of deionized water, glycerol (17904, Thermo Fisher Scientific, Inc.), and isopropanol (67-63-0, Hexeal). The tip of the extruder was located at (50, 0, and 50 mm), and thus we created an acoustic trap slightly below it at (50, 0, and 48 mm).

The purpose of this evaluation was to acquire the maximum and the minimum volumes (V_{max} and V_{min}) that could be successfully suspended by an acoustic trap with a specific target potential U_t^{tar} (-2×10^{-7} N·m ≤ $U' \leq 10 \times 10^{-7}$ N·m). Droplet volumes V were measured from captured images using an image processing package (Fiji), assuming the droplet shape was eclipse. We first generated a trap with a fixed target potential and then slowly extruded a droplet of ink (i.e., water, glycerol, or isopropanol). V_{min} was measured when the droplet volume was accumulated just enough to detach from the extruder. We kept extruding the ink until the droplet dropped or atomized and reported the value just before it happened as V_{max}. We repeated this process for all the combinations of target potentials and different inks.

Printing Process: Droplets of fluids including hydrogels, custard sauces, and UV resins were printed in a voxel-by-voxel manner. For the voxelization process, the fluids were extruded from an extruder to form a droplet at a customized flow rate. The acoustic tweezer was applied just below the nozzle to detach the fluid from the nozzle. The volume of the detached fluid droplet is controlled by the flow rate and detachment time. Then the position of the acoustic trap moves dynamically controlled by PAT to translate the trapped droplet to deposit to the target location. The distance between adjacent droplets at the same height was smaller than the droplet diameter facilitating the assembling of the droplets. Bioink, prepared as described above, was warmed to 37 °C before printing while other inks were printed at room temperature. The acoustic traps were carefully localized to target individual droplets, and the positioning and duration of the levitation trap close to the printed structure were controlled, ensuring that each droplet was precisely placed with minimal impact on surrounding printed structures.

Printing Evaluation: Printing in the directions of 0°, 90°, and 90°-180° was evaluated by depositing 2.5 μL glycerol droplets on surfaces with varying orientations. The flow rate of extrusion and time interval of voxelization were 1 μl s^{-1} and 25 s respectively. For printing at 0°, droplets were moved above the target position and deposited downwards using gravity. They were printed into 7*7 grids (side length: 60 mm) onto an acrylic board oriented horizontally. For testing printing at 90° on a vertical surface, droplets were printed into 5 × 5 grids (side length: 40 mm) on an acrylic board oriented on the XZ plane. The surface was spread with 15% polyvinyl alcohol hydrogel to prevent the dripping of deposited droplets. Images of the deposited droplets were analyzed with custom-made software that performed image distortion correction in homography, and the centroid and equivalent contact radius of deposited droplets were measured. For testing printing at 90°-180°, droplets were printed on the curved surface of horizontally oriented cylinders with varying diameters from below. The deposition is directed toward the center of the cylinder.

Bioprinting: Bioink with HOB cells embedded in 5Alg/3Gel was printed on a horizontal substrate with a droplet volume of 7 μL. A sample was printed by depositing 9 droplets of bioinks adjacently and post-printing crosslinking was performed by submerging the samples in 100 mM CaCl$_2$ solutions for 10 min. The cross-linked samples were then moved to 48-well plates for further analysis.

In Vitro Biocompatibility Assessment: Cell viability was evaluated using the Live/Dead Viability/Cytotoxicity Kit (L-3244) obtained from Invitrogen. Staining solutions were prepared by mixing calcein AM (1 μL mL^{-1}) and ethidium homodimer-1 (1 μL mL^{-1}) in culture media. Specimens were submerged in the staining solution for 30 min and then imaged using an epifluorescence microscope (Olympus IX51 Microscope). The number of live and dead cells was quantified using Fiji. For each experimental group, four replicate samples were prepared, and three images per sample were analyzed to assess cell viability.

Statistical Analysis: Statistical analysis was performed with an unpaired two-tailed t-test. A p-value smaller than 0.05 was considered as statistically significant.

Supporting Information

Supporting Information is available from the Wiley Online Library or from the author.

Acknowledgements

Conflict of Interest

The authors declare no conflict of interest.

Data Availability Statement

The data that support the findings of this study are available in the supplementary material of this article.

Keywords

3D printing, acoustic levitation, in situ printing, multi-material, omnidirectional

[1] A. Lenshof, T. Laurell, *Encyclopedia of Nanotechnology*, (eds B. Bhushan), Springer, Netherlands **2014** pp. 1–6.

[2] T. Fushimi, A. Marzo, B. W. Drinkwater, T. L. Hill, *Appl. Phys. Lett.* **2019**, *115*, 064101.

[3] Y. Koroyasu, T.-V. Nguyen, S. Sasaguri, A. Marzo, I. Ezcurdia, Y. Nagata, T. Yamamoto, N. Nomura, T. Hoshi, Y. Ochiai, T. Fushimi, *PNAS Nexus* **2023**, *2*, pgad207.

[4] C. Yin, X. Jiang, S. Mann, L. Tian, B. W. Drinkwater, *Small* **2023**, *19*, 2207917.

[5] K. Melde, H. Kremer, M. Shi, S. Seneca, C. Frey, I. Platzman, C. Degel, D. Schmitt, B. Schölkopf, P. Fischer, *Sci. Adv.* **2023**, *9*, eadf6182.

[6] K. Melde, E. Choi, Z. Wu, S. Palagi, T. Qiu, P. Fischer, *Adv. Mater.* **2018**, *30*, 1704507.

[7] L. Lu, X. Tang, S. Hu, Y. Pan, *3D Print Addit. Manufactur.* **2018**, *5*, 151.

[8] R. R. Collino, T. R. Ray, L. M. Friedrich, J. D. Cornell, C. D. Meinhart, M. R. Begley, *Mater. Res. Lett.* **2018**, *6*, 191.

[9] Y. Wang, C. Xu, J. Liu, H. Pan, Y. Li, D. Mei, *Addit. Manufactur.* **2022**, *60*, 103247.

[10] P. Agrawal, S. Zhuang, S. Dreher, S. Mitter, D. S. P. Ahmed, *Adv. Mater.* **2024**, *36*, 2408374.

[11] T. M. Llewellyn-Jones, B. W. Drinkwater, R. S Trask, *Smart Materials and Structur.* **2016**, *25*, 02LT01.

[12] Z. Ma, A. W. Holle, K. Melde, T. Qiu, K. Poeppel, V. M. Kadiri, P. Fischer, *Adv. Mater.* **2020**, *32*, 1904181.

[13] Y. Sriphutkiat, S. Kasetsirikul, D. Ketpun, Y. Zhou, *Sci. Rep.* **2019**, *9*, 17774.

[14] M. Habibi, S. Foroughi, V. Karamzadeh, M. Packirisamy, *Nat. Commun.* **2022**, *13*, 1800.

[15] H. Kawahara, K. Yamao, K. Oda, in *Adjunct Proc. of the 35th Annual ACM Symposium on User Interface Software and Technology* Article 99, Association for Computing Machinery, Bend, OR, USA, **2022**.

[16] A. Marzo, S. A. Seah, B. W. Drinkwater, D. R. Sahoo, B. Long, S. Subramanian, *Nat. Commun.* **2015**, *6*, 8661.

[17] A. Marzo, B. W. Drinkwater, *Proc. Nat. Acad. Sci.* **2018**, *116*, 84.

[18] R. Hirayama, D. Martinez Plasencia, N. Masuda, S. Subramanian, *Nature* **2019**, *575*, 320.

[19] M. A. B. Andrade, A. Marzo, J. C. Adamowski, *Appl. Phys. Lett.* **2020**, *116*, 250501.

[20] T. Fushimi, T. L. Hill, A. Marzo, B. W. Drinkwater, *Appl. Phys. Lett.* **2018**, *113*, 034102.

[21] H. Chen, S. Bansal, D. Martinez Plasencia, J. Huang, S. Subramanian, R. Hirayama, *Acoustophoretic in situ 3D fabrication of multi-material and porous structures*, Version 1 **2024**, https://doi.org/10.21203/rs.3.rs-4018436/v1.

[22] H. Ryuji, D. Martinez, N. Masuda, S. Sriram, *Proc. SPIE* **2020**, *11463*, 53.

[23] L. Gao, P. Irani, S. Subramanian, G. Prabhakar, D. Martinez Plasencia, R. Hirayama, *In Proceedings of the 2023 CHI Conference on Human Factors in Computing Systems (CHI '23)*, Association for Computing Machinery, New York, NY, USA **2023**, 1–14, https://doi.org/10.1145/3544548.3581016.

[24] J. Li, W. D. Jamieson, P. Dimitriou, W. Xu, P. Rohde, B. Martinac, M. Baker, B. W. Drinkwater, O. K. Castell, D. A. Barrow, *Nat. Commun.* **2022**, *13*, 4125.

[25] T. Tang, D. Joralmon, T. Anyigbo, X. Li, *J. Manuf. Sci. Eng.* **2023**, *146*, 011002.

[26] I. Ezcurdia, R. Morales, M. A. B. Andrade, A. L. P. Marzo in *ACM SIGGRAPH 2022 Conf. Proc.*, Vancouver BC Canada, August **2022**.

[27] R. Hirayama, G. Christopoulos, D. Martinez Plasencia, S. Subramanian, *Sci. Adv.* **2022**, *8*, eabn7614.

[28] H. Bruus, *Lab on a Chip* **2012**, *12*, 1014.

[29] D. Foresti, K. T. Kroll, R. Amissah, F. Sillani, K. A. Homan, D. Poulikakos, J. A. Lewis, *Sci. Adv.* **2018**, *4*, eaat1659.

[30] D. Foresti, M. Nabavi, M. Klingauf, A. Ferrari, D. Poulikakos, *Proc. Natl. Acad. Sci. USA* **2013**, *110*, 12549.

[31] A. L. Yarin, D. A. Weiss, G. Brenn, D. Rensink, *Int. J. Multiphase Flow* **2002**, *28*, 887.

[32] B. Derby, *Annu. Rev. Mater. Res.* **2010**, *40*, 395.

[33] H. Chen, B. Zhang, J. Huang, *Biophys. Rev.* **2024**, *5*, 031301.

[34] H. Chen, Y. Liu, S. Balabani, R. Hirayama, J. Huang, *Research* **2023**, *6*, 0197.

[35] C. Ni, D. Chen, Y. Yin, X. Wen, X. Chen, C. Yang, G. Chen, Z. Sun, J. Wen, Y. Jiao, C. Wang, N. Wang, X. Kong, S. Deng, Y. Shen, R. Xiao, X. Jin, J. Li, X. Kong, Q. Zhao, T. Xie, *Nature* **2023**, *622*, 748.

[36] H. Yang, D. Luo, K. Qian, L. Yao, in *Proceedings of the 2021 CHI Conference on Human Factors in Computing Systems* Article 620, Association for Computing Machinery, Yokohama, Japan, **2021**.

[37] A. D. Valentine, T. A. Busbee, J. W. Boley, J. R. Raney, A. Chortos, A. Kotikian, J. D. Berrigan, M. F. Durstock, J. A. Lewis, *Adv. Mater.* **2017**, *29*, 1703817.

[38] T. Fushimi, A. Marzo, T. L. Hill, B. W. Drinkwater, *2018 IEEE Int. Ultrasonics Symposium (IUS)*, Kobe, Japan, October **2018**.

[39] S. V. Murphy, A. Atala, *Nat. Biotechnol.* **2014**, *32*, 773.

[40] H. Wang, Y. Xia, Z. Zhang, Z. Xie, *J. Mater. Chem. B* **2023**, *11*, 8883.

[41] P. A. G. S. Giachini, S. S. Gupta, W. Wang, D. Wood, M. Yunusa, E. Baharlou, M. Sitti, A. Menges, *Sci. Adv.* **2020**, *6*, eaay0929.

[42] R. Montano-Murillo, R. Hirayama, D. M. Plasencia, *ACM Trans. Graph.* **2023**, *42*, 1.

[43] D. M. Plasencia, R. Hirayama, R. Montano-Murillo, S. Subramanian, *ACM Trans. Graph.* **2020**, *39*, 138.

[44] H. Chen, G. Gonnella, J. Huang, L. Di-Silvio, *Biomimetics* **2023**, *8*, 87.

[45] H. Chen, J. Khong, J. Huang, *Orthopaedic Proc.* **2021**, *103*, 74.

[46] H. Chen, T. Stampoultzis, A. Papadopoulou, S. Balabani, J. Huang, *Orthopaedic Proc.* **2021**, *103*, 96.